NANO LETTERS

pubs.acs.org/NanoLett Letter

Spin–Phonon Coupling and Magnetic Transition in an Organic Molecule Intercalated $Cr_2Ge_2Te_6$

Sudeshna Samanta, Hector Iturriaga, Thuc T. Mai, Adam J. Biacchi, Rajibul Islam, John Fullerton, Angela R. Hight Walker, Mohamed Noufal, Ryan Siebenaller, Emmanuel Rowe, Charudatta Phatak, Michael A. Susner, Fei Xue, and Srinivasa R. Singamaneni*

Cite This: *Nano Lett.* 2024, 24, 9169–9177 Read Online

ACCESS | Metrics & More | Article Recommendations | Supporting Information

ABSTRACT: The manipulation of spin–phonon coupling in both formations and explorations of magnetism in two-dimensional van der Waals ferromagnetic semiconductors facilitates unprecedented prospects for spintronic devices. The interlayer engineering with spin–phonon coupling promises controllable magnetism via organic cation intercalation. Here, spectroscopic evidence reveals the intercalation effect on the intrinsic magnetic and electronic transitions in quasi-two-dimensional $Cr_2Ge_2Te_6$ using tetrabutyl ammonium (TBA^+) as the intercalant. The temperature evolution of Raman modes, E_g^3 and A_g^1, along with the magnetization measurements, unambiguously captures the enhancement of the ferromagnetic Curie temperature in the intercalated heterostructure. Moreover, the E_g^4 mode highlights the increased effect of spin–phonon interaction in magnetic-order-induced lattice distortion. Combined with the first-principle calculations, we observed a substantial number of electrons transferred from TBA^+ to Cr through the interface. The interplay between spin–phonon coupling and magnetic ordering in van der Waals magnets appeals for further understanding of the manipulation of magnetism in layered heterostructures.

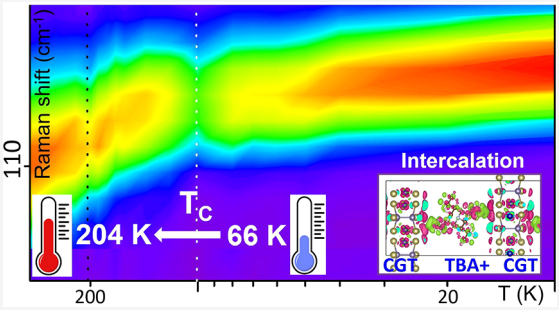

KEYWORDS: *2D magnet, organic ion intercalation, Raman spectroscopy, charge transfer, electron– and spin–phonon coupling, phonon anharmonicity*

Advancements in spintronics and valleytronics technology spur the exploration of magnetism in two-dimensional (2D) materials where charge and spin degrees of freedom of charge carriers control their intriguing properties. The recent discoveries of few-layer and monolayer 2D van der Waals (vdW) crystals such as $Cr_2Ge_2Te_6$ (CGT),[1] CrI_3,[2] and Fe_3GeTe_2[3] reveal the existence of long-range ferromagnetic order at low temperatures. However, achieving room temperature ferromagnetism involves the effective control of their magnetism by tuning the interlayer magnetic coupling with carrier doping,[4] strain,[5] pressure,[6] electric fields,[7] and photoexcitation[8] and, more recently, through cation intercalation.[9] The intercalation of foreign ions in the vdW magnet opens the possibility of manipulating magnetism and carrier dynamics by electron–phonon coupling (EPC) and spin–phonon coupling (SPC) mechanisms, respectively. Understanding these mechanisms is crucial for elucidating magnetic and thermal relaxation processes in devices, alongside multiferroelectricity.[10] The heat dissipation mechanism and magneto-elastic effects in prototype devices necessitate a comprehensive understanding of the interplay between lattice vibrations (phonons) and magnetism.

In this context, the temperature dependence of Raman spectra exhibits several prominent features correlate with spin dynamics,[11] EPC, phonon–anharmonicity, etc. Here, we probe the interfacial coupling mechanism and its close correlation with magnetic and electronic phase transitions in a quasi-2D vdW magnet and its intercalated heterostructure. Temperature-dependent Raman shifts can precisely record changes in the vibrational frequencies entangled with their lattice dynamics.

Pristine CGT is a ferromagnetic semiconductor with a band gap of ≈0.2 eV to 0.74 eV below the Curie temperature $T_C \approx$ 61–67 K (see, Figure S1).[12] The Cr^{3+} ions carry itinerant spins (S = 3/2) and local ferromagnetic moments and are octahedrally coordinated by Te ligands to form a 2D honeycomb lattice in the *ab*-plane. The individual magnetic layers are weakly stacked by vdW interactions along the *c*-axis. Prior work on an organic cation (tetrabutyl ammonium: TBA^+) intercalated CGT heterostructure (TBA-CGT) re-

Received: March 12, 2024
Revised: July 1, 2024
Accepted: July 2, 2024
Published: July 18, 2024

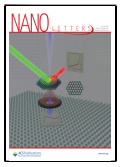

Downloaded via UNIV OF ALABAMA BIRMINGHAM on December 3, 2024 at 21:52:25 (UTC).
See https://pubs.acs.org/sharingguidelines for options on how to legitimately share published articles.

ACS Publications © 2024 American Chemical Society

https://doi.org/10.1021/acs.nanolett.4c00976
Nano Lett. 2024, 24, 9169–9177

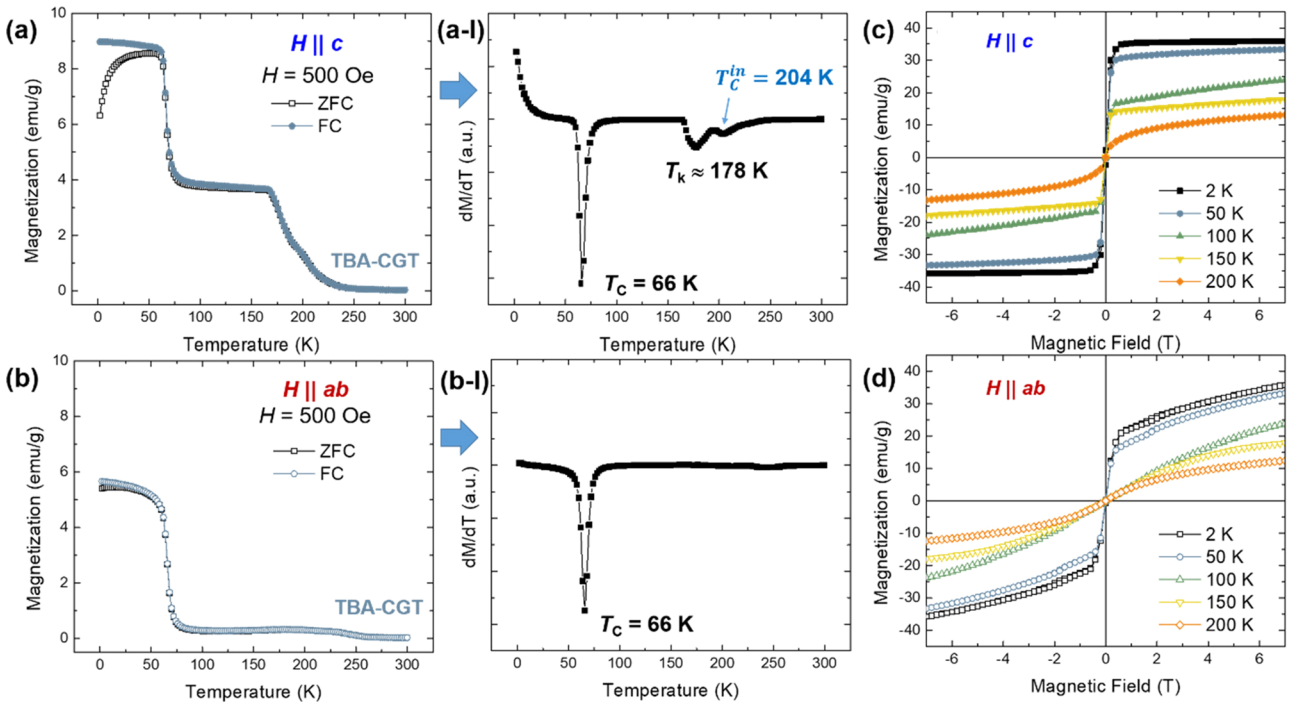

Figure 1. Temperature-dependent magnetization ($M-T$) was collected on TBA-CGT with the magnetic field (a) $H\|c$ and (b) $H\|ab$, respectively. (a)-I First derivative of the $M-T$ curve is shown in (a). (b)-I First derivative of the $M-T$ curve is shown in (b). Magnetic hysteresis ($M-H$) loops collected at a few representative temperatures under (c) $H\|c$ and (d) $H\|ab$ configurations, respectively.

ported a dramatic elevation of $T_C \approx 208$ K.[9] The magnetic easy axis flipped from the ⟨001⟩ c-axis in CGT to the ab-plane in TBA-CGT due to the transformation from a weak magnetic super exchange interaction to a strong double-exchange interaction, respectively.[9] Moreover, TBA-CGT turned into a metallic state at low temperatures, showing a semiconductor−metal transition around 165 K.[9] However, how the intercalation-induced magnetism relates to SPC for potential applications remains elusive.

To that end, we investigated the temperature response of Raman modes in TBA-CGT, especially as intercalation greatly influenced the vdW interaction due to the modification in stacking order and magnetic interactions. What differentiates our study from prior literature is the use of temperature-dependent Raman spectra to track the magnetic (ferromagnetic → paramagnetic) and electronic (semiconductor → metal) transitions in pristine and intercalated structures.[9] Combining Raman spectroscopy and magnetization measurements, we provide a comprehensive platform to understand phonons with magnetic order. Finally, theoretical simulations based on the first-principles calculations have also contributed significantly to understanding intercalated CGT's electronic and magnetic properties.

The details related to the synthesis of CGT and TBA-CGT crystals and other experimental techniques are described in the experimental section. We studied their structural and bonding characteristics using high-resolution scanning transmission electron microscopy (HRSTEM), X-ray diffraction (XRD), and X-ray photoelectron spectroscopy (XPS) (see Figures S2−S4, respectively), which confirm the successful intercalation of TBA into CGT.

At hypothetical zero temperature, CGT is described as a Heisenberg ferromagnet.[1c] The ferromagnetic transition temperatures T_C in 2D and 3D cases depend primarily on the excitation gap that originates from magnetic anisotropy and magnetic exchange interactions.[13] Therefore, ion-mediated electrochemical intercalation alters CGT's interplanar magnetic exchange interactions, providing an ideal platform for studying the magnetic ground state and SPC mechanism.

MAGNETIC ANISOTROPY-DRIVEN MAGNETIC PHASE TRANSITIONS

To describe ferromagnetism in TBA-CGT, we plot the temperature-dependent magnetization ($M-T$) in Figure 1(a) and Figure 1(b) when the applied magnetic field is along the $H\|c$ axis and $H\|ab$ plane, respectively. The derivative of magnetization (dM/dT) in Figure 1(a)-I shows ferromagnetic ordering at Curie temperature $T_C^{in} \approx 204$ K in TBA-CGT and agrees well with 208 K reported earlier.[9] Strikingly, upon cooling, two consecutive minima in dM/dT curve around $T_k \approx 178$ K and at the Curie temperature $T_C \approx 66$ K[9,14] are distinguishable and absent (see Figure 1(b)-I) when measured under $H\|ab$ plane configuration. We note that $T_k \approx 178$ K was not reported in the literature for TBA-intercalated CGT,[9] while $T_C \approx 66$ K represents the ferromagnetic ordering temperature of CGT.

The transition temperatures T_C^{in} and T_k reflect the actual effect of ion migration and its impact on quasi-2D ferromagnetic order in CGT. First, these temperatures depend purely on the crystal lattice because the ions do not bond strongly with the CGT layers. Second, TBA^+ did not affect the intrinsic T_C, and the observation of T_C^{in} is unambiguously strong evidence of a long-range secondary 2D ferromagnetism originating from the alteration of CGT atomic layers.

The strong effect of magnetic anisotropy is revealed by the isothermal magnetization ($M-H$ curves) measurements conducted at various temperatures as shown in Figure 1(c,d). TBA-CGT possesses a typical ferromagnetic behavior

https://doi.org/10.1021/acs.nanolett.4c00976
Nano Lett. 2024, 24, 9169−9177

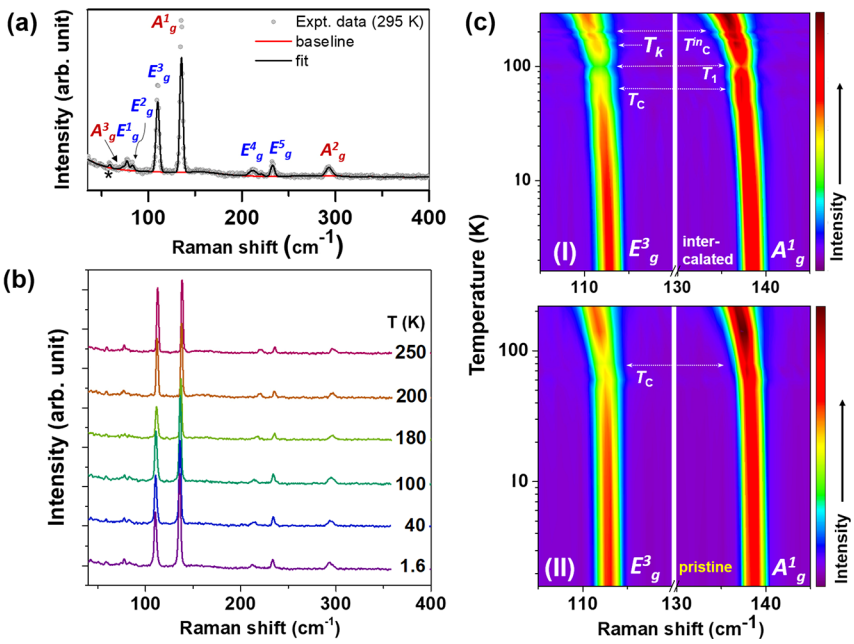

Figure 2. (a) Raman spectrum with the identified vibrational modes measured at the temperature of 295 K and (b) the temperature evolution of Raman spectra measured from 1.6 to 250 K for TBA-CGT. A mode marked as "*" in (a) represents the activated A_{2u} mode (Raman inactive) and might be a part of the Davydov doublet. (c) 2D contour map of Raman spectra (E_g^3 and A_g^1 modes) for the (I) intercalated and (II) pristine CGT ranging from 1.6 to 295 K (see text).

with a very low saturation magnetic field (≈0.5 T) at the lowest temperature of 2 K when $H \| c$ (easy axis). In contrast, when $H \| ab$ (hard axis), no saturation of the magnetization exists even at the highest magnetic field of 7 T. With increasing temperature, the change in the curvature of the $M-H$ loop indicates the onset of ferromagnetic−paramagnetic transition above 200 K. The magnetic anisotropy constant (K_u) for TBA-CGT and pristine CGT (see Figure S5) along the magnetic hard axis ($H \| ab$) decreases significantly after intercalation. Moreover, the magnetic easy axis does not change from the c-axis to the ab-plane upon intercalation, in contrast with the earlier study.[9] It was shown earlier that heavy doping (by electrostatic gating) switches the sign of the magnetic anisotropy energy and alters the magnetic easy axis from out of plane to in plane.[7] However, in the present case, the easy axis of magnetization is stable and still preserves the long-range ferromagnetic order with a high $T_C^{in} \approx 204$ K upon TBA^+ intercalation. Similar to the present results, we recently reported that the magnetic easy axis did not change in the TBA^+-intercalated $Fe_{3-x}GeTe_2$.[15]

PHONON IMPRINTS OF MAGNETIC ORDERING

Raman spectroscopy proves invaluable for analyzing long-range magnetic order and investigating the spin−phonon coupling in magnetic transitions in 2D magnetic materials,[16] such as CGT (rhombohedral crystal structure[1b] as $R\bar{3}(C_{3i}^2)$), which exhibits 10 Raman active modes as $\Gamma = 5E_g + 5A_g$.[6a,17] A typical Raman spectrum for TBA-CGT at 295 K (Figure 2(a) and Table S1) and its temperature (1.6 to 250 K) evolution are depicted in Figure 2(b), tracking the most intense modes E_g^3 and A_g^1. In CGT, low-frequency (<150 cm^{-1}), midfrequency (180−240 cm^{-1}), and high-frequency (>260 cm^{-1}) modes are dominated by motions of Te, Cr, and Ge atoms, respectively.[6a,17b] Despite noise interference, a low-frequency Raman inactive mode A_{2u} around 58.9 cm^{-1} is noted and might be a part of the Davydov doublet due to a resonant effect.[18]

After a closer inspection of the two-dimensional intensity contour plots, it is observed that E_g^3 and A_g^1 modes in TBA-CGT (see Figure 2(c)-I) and CGT (see Figure 2(c)-II) exhibit nonlinear temperature dependencies. In TBA-CGT, the modes red-shift with decreasing temperature and display several corrugated or kink-like features at discrete temperatures; T_C^{in} (≈204 K), T_k (≈178 K), T_1 (≈102 K) (discussed below), and T_C (≈66 K). Remarkably, these temperatures coincide with the temperature minima in the dM/dT curve in Figure 1(a)-I. In contrast, in CGT, only one kink-like feature is present for both modes around T_C (≈66 K) (see Figure 2(c)-II) where frequencies shift smoothly to higher energy. The rapid reduction in the intensity ratio of E_g^3 and A_g^1 modes with increasing temperature suggests that the in-plane vibrations dominate over the out-of-plane vibrations (see Figure 2(b, c)), and changes in the phonon mode intensities are associated with the magnetic orders of these 2D materials.

Notably, a recent study indicates that the distinct changes in the slope and intensity of the Raman mode frequencies around 180 K[19] occurred due to the short-range ordering of the spins in CGT, coinciding with $T_k \approx 178$ K, a feature highly discernible only in TBA-CGT. Therefore, we suggest that intercalation induces strong short-range spin ordering in TBA-CGT compared to CGT.

SPIN−PHONON COUPLING AND MAGNETIC EXCHANGE MECHANISM

In TBA-CGT, all Raman modes shift to lower wavenumbers (see Figure 3(a)), confirming the electron doping in CGT.[20] We propose that with TBA^+ intercalation, some of the Cr^{3+} ions are replaced by Cr^{2+} ions (local cation doping), potentially initiating a double-exchange mechanism. Cooling supports energetically favorable hopping across Cr^{3+}−Te−Cr^{2+} sites in CGT and stabilizes the magnetic order.[9] It preserves the

https://doi.org/10.1021/acs.nanolett.4c00976
Nano Lett. 2024, 24, 9169−9177

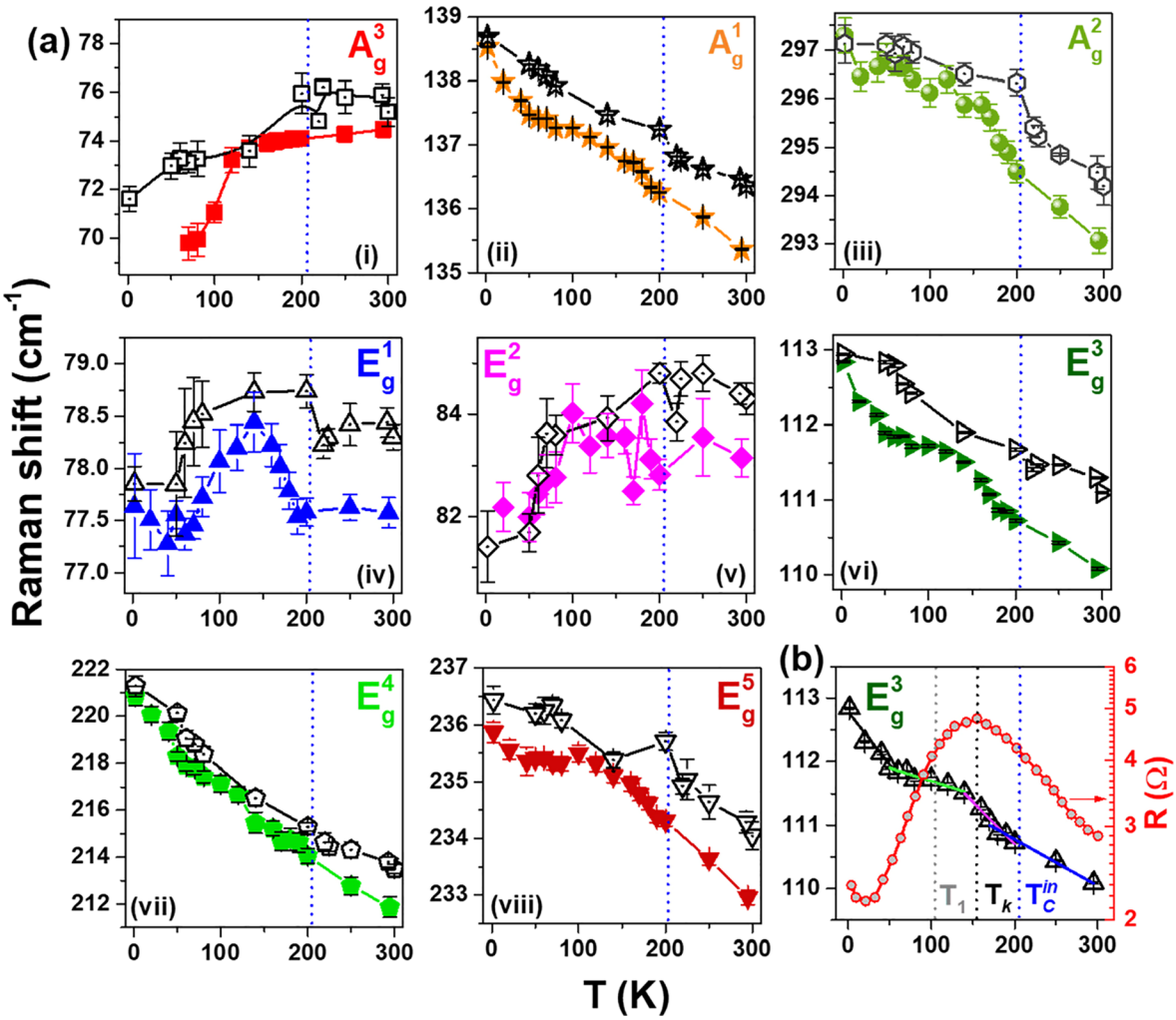

Figure 3. (a) The temperature evolution of Raman vibrations of [(i) − (iii)] A_g and [(iv) − (viii)] E_g modes in CGT (open symbols) and TBA-CGT (solid symbols). (b) Temperature dependency of the E_g^3 mode has been plotted with resistance for TBA-CGT to show the emergence of a semiconductor−metal transition around T_k. The resistance values are extracted from ref 9. Solid lines depict the linear fits to the data (see text).

electron spins in the system, and a remarkable semiconductor−metal transition occurs around T_k in sharp contrast to the semiconducting character in CGT.[9] The above conjecture supports the development of the short-range spin ordering due to intercalation.[19,21] First-order electronic transition in TBA-CGT occurs by the carrier-mediated indirect exchange mechanism through Cr^{3+}−Te−Cr^{2+} links, where the charge transfer happens by localized electrons. Additionally, the considerable ferromagnetic exchange interaction arises from the competition between the negative direct exchange (Cr^{3+}−Cr^{3+} sites) and the positive super exchange (Cr^{3+}−Te−Cr^{3+}) interactions.[17b] Further, TBA^+ intercalation causes lattice expansion along the *c*-axis, which weakens the interlayer nearest Cr's exchange interaction. It enhances SPC in the CGT layers nearest to the TBA interfaces, thereby simultaneously tuning the electrical transport and magnetic order. E_g^3 and A_g^1 modes involve the intralayer Te motions around Cr atoms in the *ab*-plane during different magnetic exchange interactions, which explains why they are highly susceptible to temperature. The red shift of the E_g^3 mode indicates the compression of the associated bonds, akin to chemical pressure-induced intercalation effects observed in high-pressure studies.[22] Thus, electron doping impacts the in-plane phonon vibrations, revealing a quasi-2D electron−phonon interaction above T_1 ≈ 102 K.[14,23] The electron spin resonance (ESR) and ferromagnetic resonance (FMR) spectroscopic studies on CGT evidenced a gradual onset of the short-ranged ferromagnetic correlation at 100 K ($H \| c$), well above the magnetic phase transition.[23] Such correlation continuously grows and slows down around T_C for $H \| c$. They also observed the resonance line shift from the paramagnetic position below 100 K, indicating an increasingly static net magnetization arising from ferromagnetic coupling between spins.

■ CATION INTERCALATION-INDUCED ELECTRON DOPING

Raman frequencies follow nonlinear temperature dependencies (see Figure 3(a) (i-viii)), exemplified by the E_g^3 mode, and are plotted simultaneously with its electrical resistance (Figure 3(b)).[9] The slope changes occur at various rates (−0.007 cm^{-1}/K, −0.015 cm^{-1}/K, −0.004 cm^{-1}/K, and −0.017 cm^{-1}/K), encompassing the electronic and magnetic transitions in the materials. In contrast, CGT's E_g^3 mode remains less sensitive (−0.003 cm^{-1}/K for 100−300 K[6a,17a]) or changes monotonically with temperature. Certain modes like A_g^3, E_g^2, and E_g^1 involving the Te atom motions around Cr atoms remain robust against temperature and exhibit blue-shift below

https://doi.org/10.1021/acs.nanolett.4c00976
Nano Lett. 2024, 24, 9169−9177

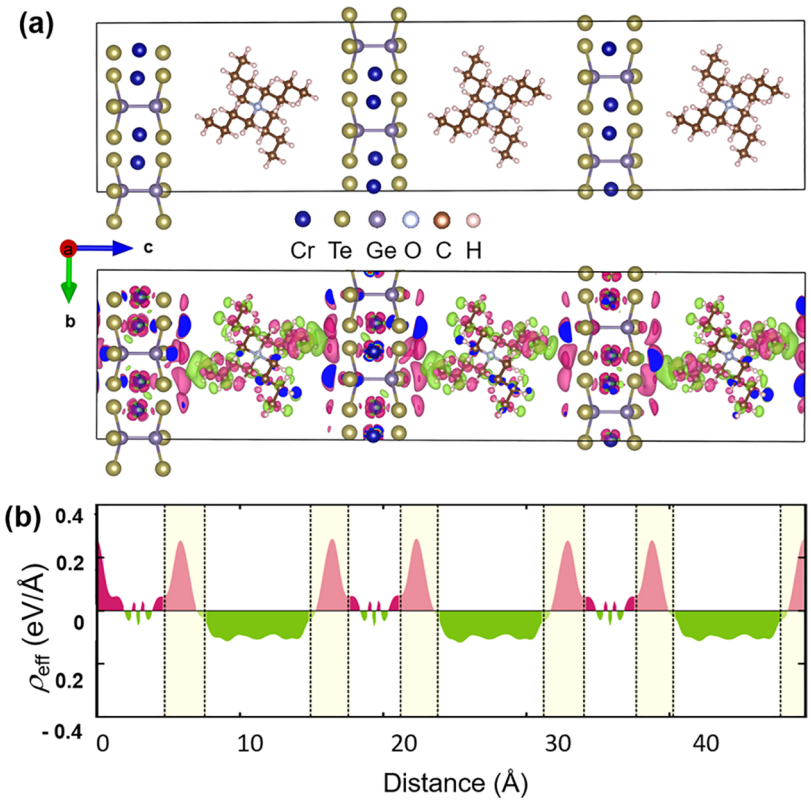

Figure 4. (a) Relaxed TBA-CGT heterostructure and isosurface charge density difference from first-principles calculations. (b) Linear charge change ($\triangle\rho_{eff}(z)$) as a function of heterostructure distance. Note that we plot the charge density difference of intercalated TBA-CGT in both isosurface and linear charge density plots to illustrate the prominent charge transfer between TBA layers and Cr atoms.

T_C^{in}, suggesting bond compression due to the intercalated cations.

As hinted above, the electrochemical cation intercalation-induced electron doping resembles an electrostatic gating effect.[7] If the intercalation is fully realized, the high-density and localized electrons are available between monolayers, and additional electrons at the interfaces generally give rise to a charge transfer between the layers. We define the linear charge density of electrons as $\rho_{eff}(z)$ and summed over the *xy*-plane per unit length such that $\int\rho_{eff}(z)dz$ is equal to the number of electrons. In Figure 4, we plot the charge density change ($\Delta\rho(z) = \rho_{CGT/TBA+}(z) - \rho_{CGT}(z) - \rho_{TBA+}(z)$) obtained from our density functional theory calculations. These results show a substantial electron transfer from TBA^+ to Cr through the interface, including charge accumulation near the interfaces (numerical values provided in Table S2), corroborating our experimental findings. We also calculated electronic band structure in the CGT/TBA^+ heterostructure,[9] and a semiconductor−metal transition occurred with intercalation, with metallic band contribution at the Fermi level (see Figure S6 (left panel)) mainly from the Cr-*d* and Te-*p* orbitals (see Figure S6 (right panel)).

The magnetic transition mechanism depends on the strength of SPC via the involvement of the Cr motion in each vibrational frequency.[17b,24] Hence, E_g^4 and E_g^2 modes have the largest SPC, about 3.19 and 1.24 cm^{-1}, respectively.[17b] The rest of the Raman modes have weak SPC coefficients involving Ge or Te atoms. Interestingly, the temperature dependency of E_g^4 mode (antiphase motions of the Cr atoms) for both samples are qualitatively different (linear temperature dependency) from their own E_g counterparts. The E_g^4 mode in TBA-CGT differs from CGT and softens faster (−0.034 cm^{-1}/K) than CGT (−0.011 cm^{-1}/K) possibly due to lattice,[6a] onset of ferromagnetic order, and increased SPC strength below 204 K (see Figure 2(a)). It also explains the direct impact of intercalation on temperature-dependent lattice shrinkage and magnetic order-induced lattice distortion.

■ ELECTRON−PHONON COUPLING AND PHONON ANHARMONICITY

Temperature evolution of Raman shifts can be expressed as $\omega(T) = \omega_0 + \Delta\omega_{vol}(T) + \Delta\omega_{anh}(T)$ where $\Delta\omega_{vol}(T)$ and $\Delta\omega_{anh}(T)$ are the volume/implicit and the true/explicit anharmonicity counterparts, respectively.[25] The solid lines in Figure 5(a) show the best fit (extended Klemens−Hart−Aggarwal−Lax phonon decay model of phonons) to the experimental data applied for $T_C < T < T_C^{in}$ in TBA-CGT (Supporting Information, Table S3).

The modes in the paramagnetic phase ($T > T_C^{in}$) strongly deviate from the Boltzmann-sigmoidal fits. We calculate spin−phonon interaction parameters $\lambda' = \frac{\Delta\omega}{\langle S_i \cdot S_j \rangle}$ for E_g^3, A_g^1, and E_g^4 for TBA-CGT and CGT (Table S3), where $\Delta\omega$ is the frequency difference at the lowest temperature (0 K) and T_C^{in}; *S* is spin on the magnetic ion/site; $\langle S_i \cdot S_j \rangle$ is the spin−spin correlation function between the ith and j^{th} site of the magnetic ions; and $S = 3/2$ for the Cr^{3+} magnetic ion.[17a] The negative values of λ' indicate the hardening of the phonon frequencies with a reduction of the temperatures up to 1.5 K. λ' is higher for E_g^4 compared to E_g^3 and A_g^1 in TBA-CGT. It reconfirms the

https://doi.org/10.1021/acs.nanolett.4c00976
Nano Lett. 2024, 24, 9169−9177

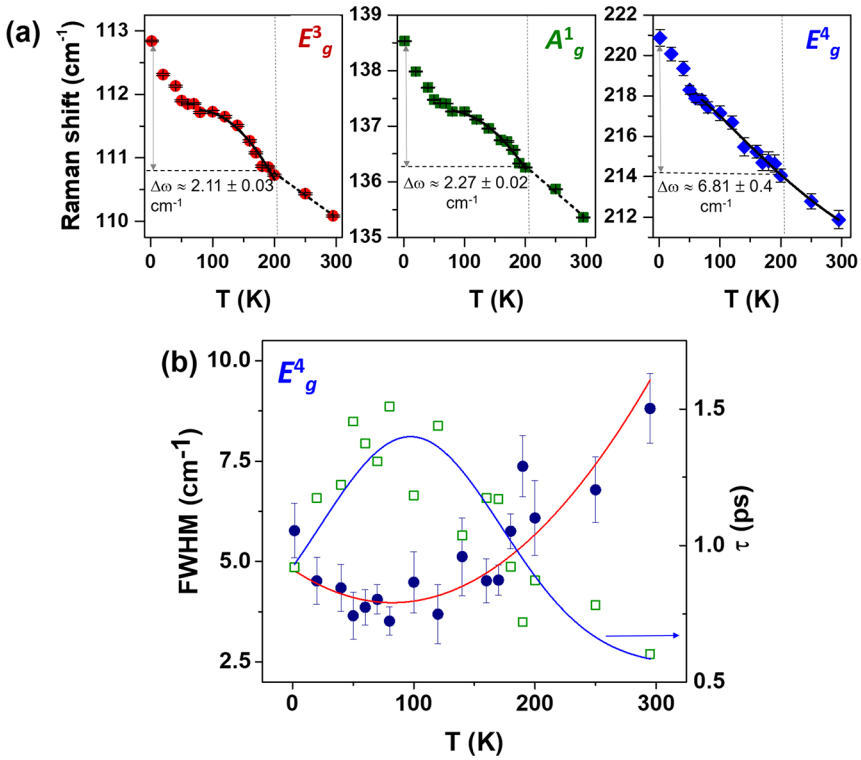

Figure 5. (a) Temperature dependence of phonon frequency shifts for TBA-CGT. The solid line shows the model fits discussed in the texts. The vertical dash line indicates T_C. (b) Temperature variation of full width at half-maximum (FWHM) (circles in blue) and phonon lifetime (open squares in green) for TBA-CGT have been plotted together for the E_g^4 mode. The electron−phonon coupling, along with the three- and four-phonon scattering terms, fitted for E_g^4 mode (red solid curve). The phonon lifetime is fitted with the Gaussian curve (blue solid curve).

substantial modification of the exchange coupling after intercalation.

Here, we reveal a close correlation between EPC and a sharp drop of resistance around $T_1 \approx 100$ K in TBA-CGT.[9] The extracted E_g^4 mode line width (FWHM: the full-width at half-maximum) as a function of temperature shows anomalous and distinctly nonlinear characteristics (see Figure 5 (b), Supporting Information). In the presence of strong EPC, a rapid reduction in line width occurs below 100 K. The EPC strength at a hypothetical absolute zero temperature is estimated as $\Gamma_{EPC}(0) \approx 3.72 \pm 0.31$ cm^{-1}. Around and below $T_1 \approx 100$ K, the phonon lifetime $\tau = \frac{1}{2\pi c(\mathrm{FWHM})}$ is the longest, about 1.1−1.5 ps, where c is the velocity of the light. A recent THz spectroscopy study on CGT reported $\tau \approx 1.15$−1.11 ps[26] along with an attenuation of FWHM due to the formation of magnetic correlations below the spin fluctuation temperature of 160 K.[26] In pristine CGT, it has been reported that lattice parameter α demonstrates the onset of a negative thermal expansion around T_1.[1b,27] Hence, we can infer that the enhancement of τ of in-plane vibration (E_g^4 mode) (see Figure 5 (b)) occurs due to the reduced phonon−phonon interactions because of lattice expansion in the *ab*-plane with decreasing temperature. However, τ decreases due to the increased phonon−phonon scattering events at higher temperatures. For the other modes, only phonon−phonon interaction exists without any EPC. We suggest that EPC triggers the semiconductor−metal transition in TBA-CGT, producing a sharp resistance drop around T_1.

The time-reversal symmetry breaking lifts degeneracy, causing splitting the lowest energy phonon mode (E_g^1: 78.6 cm^{-1}) in CGT at low temperatures, originating from the Cr^{3+}−Te−Cr^{3+} superexchange mechanism.[17a,21] Due to the weak intensity, broadness of the peak, and limitation of the spectral resolution, it would be erroneous to estimate the exact temperature at which the splitting occurs (see Figure S7), and splitting grows as magnetic order sets in near T_C. Strong SPC with a Cr^{3+}−Te−Cr^{2+} configuration hinders the phonon splitting at low temperatures in TBA-CGT, indicating a shift from super exchange to double exchange after intercalation. Background Raman scattering (a large magnetic quasi-electron scattering signal) also dramatically changes at transition temperatures (see Figure S7 and Figure S8), confirming the quasi-2D nature of magnetism of intercalated CGT.[17a]

By investigating the temperature-dependent Raman spectra in an intercalated quasi-2D vdW magnetic TBA-CGT, we analyzed the spin−phonon and electron−phonon coupling mechanisms, closely linked to magnetic exchange interaction. Upon cooling, E_g^3 and A_g^1 Raman modes display temperature-dependent changes consistent with magnetization measurements, elevating ferromagnetic Curie temperature and semiconductor−metal transition in the intercalated CGT. The E_g^4 phonon mode with the largest SPC constant (largest intraplanar Cr^{3+} motions) correlates with the existence of strong electron−phonon coupling during the electronic transition. The magnetic easy axis remains unchanged in TBA-CGT, while the magnetic interaction changes from super exchange to double exchange through Cr^{3+}−Te−Cr^{2+} links. This study provides insights into tunable SPC dynamics in 2D magnetic materials pertinent for spin-related applications like spin filtering, spin Seebeck effect, spin wave control, etc.

Sample Synthesis. We fabricated $Cr_2Ge_2Te_6$ using a flux growth reaction using Cr powder, Ge, and Te pieces in the ratio 2:6:36 with an Al_2O_3 frit (LSP ceramics[28]). The details of

https://doi.org/10.1021/acs.nanolett.4c00976
Nano Lett. 2024, 24, 9169−9177

the synthesis are described in the Supporting Information. We recorded the discharge curve during the electrochemical discharge process during TBA^+ intercalation (see Figure S2).

Sample Characterization: X-ray Diffraction (XRD). We took room temperature X-ray powder diffraction of the material's (00*l*) face with a Bruker D8 Discover system using Cu-K_α radiation ($^{\bullet}\lambda$ = 1.78897 Å) (see Figure S3) (Supporting Information).

X-ray Photoelectron Spectroscopy (XPS). XPS was performed using a Kratos Axis Ultra system with a monochromatic Al-K_α excitation source operating at 15 kV and 10 mA (Supporting Information, see Figure S4). The native surface oxide layer of CGT and TBA-CGT was removed using Ar^+ sputtering prior to photoelectron collection. Data analysis was conducted with Shirley's backgrounds using CasaXPS.

Magnetometry. For TBA-CGT, low-temperature bulk magnetometry measurements in-plane ($H \| b$) and out-of-plane ($H \| c$) of the magnetic field were conducted using a Quantum Design Physical Property Measurement System with the AC Measurement System option. We extracted DC moment data in a temperature range extending from 5 to 200 K and a maximum magnetic field of ±30 kOe.

Raman Spectroscopy. Raman measurements were performed in the parallel polarization configuration on the bulk crystals in the 1.5−295 K temperature range. Raman measurements were performed in the parallel polarization configuration using an Attocube 2100 cryostat coupled to a Horiba T64000 spectrometer. The bulk crystal was probed with 514 nm excitation at a power below 1 mW focused through a 50× objective.

Theoretical Calculations. Electronic structure calculations were performed within the framework of density functional theory using the projector augmented wave method and the VASP package.[29] We use the generalized gradient approximation (GGA) method[30] with intrasite Hubbard *U* for Cr *d*-electrons (Supporting Information).[31] The total energy was converged to 10^{-8} eV with a Gaussian-smearing method. We calculated using a 4 × 4 × 1 Γ-centered *k*-mesh with 16 *k*-points in the Brillouin zone.

■ ASSOCIATED CONTENT

Supporting Information

The Supporting Information is available free of charge at https://pubs.acs.org/doi/10.1021/acs.nanolett.4c00976.

> Temperature-dependent magnetization curves, X-ray diffraction, high-resolution scanning transmission electron microscopy and X-ray photoelectron spectroscopy for all compounds, details of theoretical model fitting and quasi-electron scattering in Raman spectra, details of theoretical band structure calculations, and additional details of sample synthesis (PDF)

■ AUTHOR INFORMATION

Corresponding Author

Srinivasa R. Singamaneni − *Department of Physics, The University of Texas at El Paso, El Paso, Texas 79968, United States*; Email: srao@utep.edu

Authors

Sudeshna Samanta − *Department of Physics, The University of Texas at El Paso, El Paso, Texas 79968, United States*; orcid.org/0000-0001-7341-3808

Hector Iturriaga − *Department of Physics, The University of Texas at El Paso, El Paso, Texas 79968, United States*

Thuc T. Mai − *Quantum Measurement Division, Physical Measurement Laboratory, National Institute of Standards and Technology, Gaithersburg, Maryland 20899, United States*

Adam J. Biacchi − *Nanoscale Device Characterization Division, Physical Measurement Laboratory, National Institute of Standards and Technology, Gaithersburg, Maryland 20899, United States*; orcid.org/0000-0001-5663-2048

Rajibul Islam − *Department of Physics, University of Alabama at Birmingham, Birmingham, Alabama 35233, United States*; orcid.org/0000-0001-9076-7843

John Fullerton − *Materials Science Division, Argonne National Laboratory, Lemont, Illinois 60439, United States*; orcid.org/0000-0002-7527-7034

Angela R. Hight Walker − *Quantum Measurement Division, Physical Measurement Laboratory, National Institute of Standards and Technology, Gaithersburg, Maryland 20899, United States*; orcid.org/0000-0003-1385-0672

Mohamed Noufal − *Department of Chemical Engineering, Hampton University, Hampton, Virginia 23668, United States*

Ryan Siebenaller − *Materials and Manufacturing Directorate, Air Force Research Laboratory, Wright-Patterson Air Force Base, Ohio 45433, United States; Department of Materials Science and Engineering, The Ohio State University, Columbus, Ohio 43210, United States*

Emmanuel Rowe − *Department of Materials Science and Engineering, The Ohio State University, Columbus, Ohio 43210, United States; National Research Council, Washington, D.C. 20001, United States; Department of Engineering Technology, Middle Tennessee State University, Murfreesboro, Tennessee 37132, United States; Department of Astronomy and Physics, Vanderbilt University, Nashville, Tennessee 37235, United States; Department of Life and Physical Sciences, Fisk University, Nashville, Tennessee 37208, United States*

Charudatta Phatak − *Materials Science Division, Argonne National Laboratory, Lemont, Illinois 60439, United States; Department of Materials Science and Engineering, Northwestern University, Evanston, Illinois 60208, United States*; orcid.org/0000-0002-8931-0296

Michael A. Susner − *Materials and Manufacturing Directorate, Air Force Research Laboratory, Wright-Patterson Air Force Base, Ohio 45433, United States*

Fei Xue − *Department of Physics, University of Alabama at Birmingham, Birmingham, Alabama 35233, United States*

Complete contact information is available at: https://pubs.acs.org/10.1021/acs.nanolett.4c00976

Author Contributions

The manuscript was written with contributions from all authors. All authors have approved the final version of the manuscript

Notes

The authors declare no competing financial interest.

https://doi.org/10.1021/acs.nanolett.4c00976
Nano Lett. 2024, 24, 9169−9177

NIST co-authors declare that certain commercial equipment, instrumentation, or materials are identified in this document to adequately specify the experimental procedures. Such identification does not imply recommendation or endorsement by the National Institute of Standards and Technology, nor does it imply that the products identified are necessarily the best available for the purpose.

■ ACKNOWLEDGMENTS

This material is based upon work supported by the National Science Foundation Graduate Research Fellowship Program under Grant No. 184874.1. Any opinions, findings, and conclusions or recommendations expressed in this material are those of the author(s) and do not necessarily reflect the views of the National Science Foundation. S.R.S. and H.I. acknowledge support from the NSF-DMR (Award No. 2105109). S.R.S. acknowledges support from NSF-MRI (Award No. 2018067). We acknowledge the support of the Air Force Office of Scientific Research (AFOSR) Grant Nos. LRIR 23RXCOR003 and AOARD MOST, Grant No. F4GGA21207H002, as well as general support from the Air Force Materials and Manufacturing (R.X.), Sensors (R.Y.), and Aerospace Systems (R.Q.) Directorates. R.I. and F.X acknowledge the support by the National Science Foundation under Grant No. OIA-2229498 and Oak Ridge Associated Universities Ralph E. Powe Junior Faculty Enhancement Award. We also acknowledge support from the National Research Council's Senior NRC Associateship program sponsored by the National Academies of Sciences, Engineering, and Medicine. Work by J.F. and C.P. was funded by the US Department of Energy, Office of Science, Office of Basic Energy Sciences, Materials Science and Engineering Division. Work performed at the Center for Nanoscale Materials, a U.S. Department of Energy, Office of Science User Facility, was supported by the U.S. DOE, Office of Basic Energy Sciences, under contract no. DE-AC0206CH11357.

■ REFERENCES

(1) (a) Williams, T. J.; Aczel, A. A.; Lumsden, M. D.; Nagler, S. E.; Stone, M. B.; Yan, J. Q.; Mandrus, D. Magnetic correlations in the quasi-two-dimensional semiconducting ferromagnet CrSiTe3. *Phys. Rev. B* **2015**, *92* (14), 144404. (b) Carteaux, V.; Brunet, D.; Ouvrard, G.; Andre, G. Crystallographic, magnetic and electronic structures of a new layered ferromagnetic compound Cr2Ge2Te6. *J. Phys.: Condens. Matter* **1995**, *7* (1), 69. (c) Gong, C.; Li, L.; Li, Z.; Ji, H.; Stern, A.; Xia, Y.; Cao, T.; Bao, W.; Wang, C.; Wang, Y.; Qiu, Z. Q.; Cava, R. J.; Louie, S. G.; Xia, J.; Zhang, X. Discovery of intrinsic ferromagnetism in two-dimensional van der Waals crystals. *Nature* **2017**, *546* (7657), 265−269.

(2) Huang, B.; Clark, G.; Navarro-Moratalla, E.; Klein, D. R.; Cheng, R.; Seyler, K. L.; Zhong, D.; Schmidgall, E.; McGuire, M. A.; Cobden, D. H.; Yao, W.; Xiao, D.; Jarillo-Herrero, P.; Xu, X. Layer-dependent ferromagnetism in a van der Waals crystal down to the monolayer limit. *Nature* **2017**, *546* (7657), 270−273.

(3) Zhang, G.; Guo, F.; Wu, H.; Wen, X.; Yang, L.; Jin, W.; Zhang, W.; Chang, H. Above-room-temperature strong intrinsic ferromagnetism in 2D van der Waals Fe3GaTe2 with large perpendicular magnetic anisotropy. *Nat. Commun.* **2022**, *13* (1), 5067.

(4) Jiang, X.; Liu, Q.; Xing, J.; Liu, N.; Guo, Y.; Liu, Z.; Zhao, J. Recent progress on 2D magnets: Fundamental mechanism, structural design and modification. *Applied Physics Reviews* **2021**, *8* (3), 031305.

(5) Liu, P.; Zhang, Y.; Li, K.; Li, Y.; Pu, Y. Recent advances in 2D van der Waals magnets: Detection, modulation, and applications. *iScience* **2023**, *26* (9), 107584.

(6) (a) Sun, Y.; Xiao, R. C.; Lin, G. T.; Zhang, R. R.; Ling, L. S.; Ma, Z. W.; Luo, X.; Lu, W. J.; Sun, Y. P.; Sheng, Z. G. Effects of hydrostatic pressure on spin-lattice coupling in two-dimensional ferromagnetic Cr2Ge2Te6. *Appl. Phys. Lett.* **2018**, *112* (7), 072409. (b) Yu, Z.; Xia, W.; Xu, K.; Xu, M.; Wang, H.; Wang, X.; Yu, N.; Zou, Z.; Zhao, J.; Wang, L.; Miao, X.; Guo, Y. Pressure-Induced Structural Phase Transition and a Special Amorphization Phase of Two-Dimensional Ferromagnetic Semiconductor Cr2Ge2Te6. *J. Phys. Chem. C* **2019**, *123* (22), 13885−13891. (c) Olmos, R.; Alam, S.; Chang, P.-H.; Gandha, K.; Nlebedim, I. C.; Cole, A.; Tafti, F.; Zope, R. R.; Singamaneni, S. R. Pressure dependent magnetic properties on bulk CrBr3 single crystals. *J. Alloys Compd.* **2022**, *911*, 165034. (d) Olmos, R.; Chang, P.-H.; Mishra, P.; Zope, R. R.; Baruah, T.; Liu, Y.; Petrovic, C.; Singamaneni, S. R. Pressure-Dependent Magnetic Properties of Quasi-2D Cr2Si2Te6 and Mn3Si2Te6. *J. Phys. Chem. C* **2023**, *127* (21), 10324−10331.

(7) Verzhbitskiy, I. A.; Kurebayashi, H.; Cheng, H.; Zhou, J.; Khan, S.; Feng, Y. P.; Eda, G. Controlling the magnetic anisotropy in Cr2Ge2Te6 by electrostatic gating. *Nat. Electron.* **2020**, *3* (8), 460−465.

(8) (a) Singamaneni, S. R.; Martinez, L. M.; Niklas, J.; Poluektov, O. G.; Yadav, R.; Pizzochero, M.; Yazyev, O. V.; McGuire, M. A. Light induced electron spin resonance properties of van der Waals CrX3 (X = Cl, I) crystals. *Appl. Phys. Lett.* **2020**, *117* (8), 082406. (b) Padmanabhan, P.; Buessen, F. L.; Tutchton, R.; Kwock, K. W. C.; Gilinsky, S.; Lee, M. C.; McGuire, M. A.; Singamaneni, S. R.; Yarotski, D. A.; Paramekanti, A.; Zhu, J. X.; Prasankumar, R. P. Coherent helicity-dependent spin-phonon oscillations in the ferromagnetic van der Waals crystal CrI3. *Nat. Commun.* **2022**, *13* (1), 4473.

(9) Wang, N.; Tang, H.; Shi, M.; Zhang, H.; Zhuo, W.; Liu, D.; Meng, F.; Ma, L.; Ying, J.; Zou, L.; Sun, Z.; Chen, X. Transition from Ferromagnetic Semiconductor to Ferromagnetic Metal with Enhanced Curie Temperature in Cr(2)Ge(2)Te(6) via Organic Ion Intercalation. *J. Am. Chem. Soc.* **2019**, *141* (43), 17166−17173.

(10) Gong, C.; Kim, E. M.; Wang, Y.; Lee, G.; Zhang, X. Multiferroicity in atomic van der Waals heterostructures. *Nat. Commun.* **2019**, *10* (1), 2657.

(11) (a) Choe, J.; Lujan, D.; Rodriguez-Vega, M.; Ye, Z.; Leonardo, A.; Quan, J.; Nunley, T. N.; Chang, L. J.; Lee, S. F.; Yan, J.; Fiete, G. A.; He, R.; Li, X. Electron-Phonon and Spin-Lattice Coupling in Atomically Thin Layers of MnBi(2)Te(4). *Nano Lett.* **2021**, *21* (14), 6139−6145. (b) McCreary, A.; Simpson, J. R.; Mai, T. T.; McMichael, R. D.; Douglas, J. E.; Butch, N.; Dennis, C.; Valdés Aguilar, R.; Hight Walker, A. R. Quasi-two-dimensional magnon identification in antiferromagnetic FePS3 via magneto-Raman spectroscopy. *Phys. Rev. B* **2020**, *101* (6), 064416.

(12) Williams, T. J.; Aczel, A. A.; Lumsden, M. D.; Nagler, S. E.; Stone, M. B.; Yan, J. Q.; Mandrus, D. Magnetic correlations in the quasi-two-dimensional semiconducting ferromagnetCrSiTe$_3$. *Phys. Rev. B* **2015**, *92* (14), 144404.

(13) Wu, H.; Zhu, J.-X.; Chen, L.; Butcher, M. W.; Yue, Z.; Yuan, D.; He, Y.; Oh, J. S.; Gao, B.; Huang, J.; Wu, S.; Gong, C.; Guo, Y.; Mo, S.-K.; Denlinger, J.; Lu, D.; Hashimoto, M.; Stone, M. B.; Kolesnikov, A. I.; Chi, S.; Kono, J.; Nevidomskyy, A. H.; Birgeneau, R. J.; Dai, P.; Yi, M. Two-Step Electronic Response to Magnetic Ordering in a van der Waals Ferromagnet. *Phys. Rev. B* **2024**, DOI: 10.1103/PhysRevB.109.045416.

(14) Liu, Y.; Han, M. G.; Lee, Y.; Ogunbunmi, M. O.; Du, Q.; Nelson, C.; Hu, Z.; Stavitski, E.; Graf, D.; Attenkofer, K.; Bobev, S.; Ke, L.; Zhu, Y.; Petrovic, C. Polaronic Conductivity in Cr2Ge2Te6 Single Crystals. *Adv. Funct. Mater.* **2022**, *32* (19), 2105111.

(15) Iturriaga, H.; Martinez, L. M.; Mai, T. T.; Biacchi, A. J.; Augustin, M.; Hight Walker, A. R.; Sanad, M. F.; Sreenivasan, S. T.; Liu, Y.; Santos, E. J. G.; Petrovic, C.; Singamaneni, S. R. Magnetic properties of intercalated quasi-2D Fe3-xGeTe2 van der Waals magnet. *npj 2D Mater. Appl.* **2023**, *7* (1), 56.

(16) Mai, T. T.; Garrity, K. F.; McCreary, A.; Argo, J.; Simpson, J. R.; Doan-Nguyen, V.; Aguilar, R. V.; Walker, A. R. H. Magnon-

phonon hybridization in 2D antiferromagnet MnPSe3. *Science Advances* **2021**, *7* (44), eabj3106.

(17) (a) Tian, Y.; Gray, M. J.; Ji, H.; Cava, R. J.; Burch, K. S. Magneto-elastic coupling in a potential ferromagnetic 2D atomic crystal. *2D Materials* **2016**, *3* (2), 025035. (b) Zhang, B. H.; Hou, Y. S.; Wang, Z.; Wu, R. Q. First-principles studies of spin-phonon coupling in monolayer Cr2Ge2Te6. *Phys. Rev. B* **2019**, DOI: 10.1103/PhysRevB.100.224427.

(18) Song, Q. J.; Tan, Q. H.; Zhang, X.; Wu, J. B.; Sheng, B. W.; Wan, Y.; Wang, X. Q.; Dai, L.; Tan, P. H. Physical origin of Davydov splitting and resonant Raman spectroscopy of Davydov components in multilayer MoTe2. *Phys. Rev. B* **2016**, *93* (11), 115409.

(19) Chakkar, A. G.; Kumar, D.; Kumar, P. Broken weak and strong spin rotational symmetries and tunable interaction between phonon and the continuum in Cr2Ge2Te6. *Phys. Rev. B* **2024**, DOI: 10.1103/PhysRevB.109.134406.

(20) Menichetti, G.; Calandra, M.; Polini, M. Electrical tuning of the magnetic properties of 2D magnets: the case of Cr2Ge2Te6. *Phys. Rev. B* **2024**, DOI: 10.1103/PhysRevB.109.205139.

(21) Liam Trzaska, L. Q.; Watson, M. D. Charge doping into spin minority states mediates doubling of TC in ferromagnetic CrGeTe3. *arXiv:2312.00440v1* **2023**, DOI: 10.48550/arXiv.2312.00440.

(22) Ge, W.; Xu, K.; Xia, W.; Yu, Z.; Wang, H.; Liu, X.; Zhao, J.; Wang, X.; Yu, N.; Zou, Z.; Yan, Z.; Wang, L.; Xu, M.; Guo, Y. Raman spectroscopy and lattice dynamical stability study of 2D ferromagnetic semiconductor Cr2Ge2Te6 under high pressure. *J. Alloys Compd.* **2020**, *819*, 153368.

(23) Zeisner, J.; Alfonsov, A.; Selter, S.; Aswartham, S.; Ghimire, M. P.; Richter, M.; van den Brink, J.; Büchner, B.; Kataev, V. Magnetic anisotropy and spin-polarized two-dimensional electron gas in the van der Waals ferromagnet Cr2Ge2Te6. *Phys. Rev. B* **2019**, *99* (16), 165109.

(24) Chen, L.; Mao, C.; Chung, J. H.; Stone, M. B.; Kolesnikov, A. I.; Wang, X.; Murai, N.; Gao, B.; Delaire, O.; Dai, P. Anisotropic magnon damping by zero-temperature quantum fluctuations in ferromagnetic CrGeTe(3). *Nat. Commun.* **2022**, *13* (1), 4037.

(25) Samanta, S.; Gusain, M.; Zhang, Y.; Zhan, Y.; Zhang, H.; Wang, L.; Xiong, S. Deep Dive into Lattice Dynamics and Phonon Anharmonicity for Intrinsically Low Thermal Expansion Coefficient in CuS. *ChemNanoMat* **2022**, DOI: 10.1002/cnma.202200238.

(26) Cheng, L.; Li, H.; Lin, G.; Yan, J.; Zhang, L.; Yang, C.; Tong, W.; Ren, Z.; Zhu, W.; Cong, X.; Gao, J.; Tan, P.; Luo, X.; Sun, Y.; Zhu, W.; Sheng, Z. Phonon-Related Monochromatic THz Radiation and its Magneto-Modulation in 2D Ferromagnetic Cr(2) Ge(2) Te(6). *Advanced science* **2022**, *9* (1), e2103229.

(27) Yang, D.; Yao, W.; Chen, Q.; Peng, K.; Jiang, P.; Lu, X.; Uher, C.; Yang, T.; Wang, G.; Zhou, X. Cr2Ge2Te6: High Thermoelectric Performance from Layered Structure with High Symmetry. *Chem. Mater.* **2016**, *28* (6), 1611−1615.

(28) Canfield, P. C.; Kong, T.; Kaluarachchi, U. S.; Jo, N. H. Use of frit-disc crucibles for routine and exploratory solution growth of single crystalline samples. *Philos. Mag.* **2016**, *96* (1), 84−92.

(29) Kresse, G.; Furthmüller, J. Efficient iterative schemes for ab initio total-energy calculations using a plane-wave basis set. *Phys. Rev. B* **1996**, *54* (16), 11169−11186.

(30) Perdew, J. P.; Burke, K.; Ernzerhof, M. Generalized Gradient Approximation Made Simple. *Phys. Rev. Lett.* **1996**, *77* (18), 3865−3868.

(31) (a) Gonzalez Szwacki, N.; Majewski, J. A.; Dietl, T. Aggregation and magnetism of Cr, Mn, and Fe cations in GaN. *Phys. Rev. B* **2011**, *83* (18), 184417. (b) Islam, R.; Mardanya, S.; Lau, A.; Cuono, G.; Chang, T.-R.; Singh, B.; Canali, C. M.; Dietl, T.; Autieri, C. Engineering axion insulator and other topological phases in superlattices without inversion symmetry. *Phys. Rev. B* **2023**, *107* (12), 125102.

https://doi.org/10.1021/acs.nanolett.4c00976
Nano Lett. 2024, 24, 9169−9177